

22 **Abstract**

23 In the United States, severe weather poses a threat to society, producing tornadoes and hail that
24 can result in hundreds of casualties and billions of dollars in damages. Fortunately, skillful
25 predictions of severe weather for short lead times of 0–8 days and longer lead times exceeding
26 one month have been realized. However, this leaves a “forecast gap” at subseasonal to seasonal
27 (S2S) lead times of 2–5 weeks, when early-action decision making by stakeholders is typically
28 made. Here we develop an empirical prediction model that fills this gap during March–June
29 when severe weather is most prevalent across the United States. We demonstrate skillful weekly
30 forecasts of opportunity with lead times of 2–5 weeks of environmental parameters favorable to
31 severe weather, as well as actual tornado and hail activity. To attain this skill, we use as a
32 predictor the current state of active phases of the Madden-Julian Oscillation, known to have
33 physical teleconnections with future weather over the United States. The model has significant
34 skill in regions such as the Plains and the Southeast, providing stakeholders with valuable
35 extended forewarning.

36 **Plain Language Summary**

37 In the United States, severe thunderstorms produce tornadoes and large hail, responsible for
38 hundreds of deaths and injuries and many billions of dollars in damages on average each year.
39 Because of these devastating impacts, there is a keen interest to accurately forecast when and
40 where severe thunderstorms are likely to occur. While meteorologists and computer models do
41 reasonably well in forecasting severe thunderstorm activity up to a week in advance, their
42 forecasts are less reliable in the 2 to 5 week timeframe. In our study, we develop a technique that
43 can accurately forecast severe thunderstorm activity in this timeframe by using knowledge of the
44 current state of weather in the tropics. These accurate, extended forecasts offer valuable
45 forewarning to both the general public and stakeholders of when and where potentially deadly
46 severe thunderstorm activity is likely to occur.

47 **1. Introduction**

48 In the United States, severe convective storms, namely tornadoes, large hail [> 25.4 mm
49 (1 inch)], and high winds [> 25.9 m s⁻¹ (58 mph)], wreak devastation on life and property –
50 resulting in over 900 fatalities and \$125 billion in damages over the 2007–2016 period alone
51 (NOAA/NCEI, 2018; NOAA/SPC 2018). During this ten-year period, severe weather was
52 responsible for 54 billion-dollar events, more than all other natural hazards combined (e.g.,
53 flooding, droughts, and tropical cyclones; NOAA/NCEI, 2018; Smith & Matthews, 2015). Nine
54 of these 54 events occurred during 2011, including a pair of infamous, multi-day events in late
55 April and late May that collectively killed 498 people and caused \$21.6 billion in damages
56 (NOAA/NCEI, 2018) – leaving Tuscaloosa, AL and Joplin, MO devastated in their wake.

57 Because of these impacts, society and stakeholders have a keen interest in skillful
58 forecasts of when and where severe weather will occur (Allen et al., 2016; Gunturi & Tippett,
59 2017; NOAA/NCEI, 2018; Simmons & Sutter, 2011; Smith & Matthews, 2015). Fortunately,
60 tremendous progress has been made in understanding the favorable, large-scale environmental
61 conditions that promote the growth, organization, and maintenance of severe thunderstorms –
62 namely, instability, vertical shear, and convective initiation mechanisms (Allen et al., 2015a;
63 Brooks et al., 2003; Gensini & Ashley, 2011; Tippett et al., 2012, 2014, 2015). Forecasts for
64 these favorable environmental conditions are being issued and developed for a variety of time
65 scales at different forecast lead times. For example, the National Oceanic and Atmospheric
66 Administration’s Storm Prediction Center (NOAA/SPC) regularly issues skillful probabilistic,
67 daily convective outlooks (Herman et al., 2017) with forecast lead times of 0–3 days and has
68 recently begun issuing 4–8 day outlooks (available at
69 <http://www.spc.noaa.gov/products/outlook/>). For seasonal outlooks with lead times exceeding

70 one month, the El Niño/Southern Oscillation (ENSO) has been shown to influence tornado and
71 hail frequencies in the United States (Allen et al., 2015b; Childs et al., 2018; Cook et al., 2017;
72 Lepore et al., 2017). Skillful seasonal forecasts using ENSO have been demonstrated (Allen et
73 al., 2015b; Lepore et al., 2017) and are of interest to stakeholders (Gunturi & Tippett, 2017).

74 For intermediate forecast lead times of 2–5 weeks (during the subseasonal portion of the
75 so-called subseasonal to seasonal [S2S] time scale), skillful guidance for severe weather activity
76 on weekly timescales is currently in its infancy (Allen et al., 2016; Barrett & Gensini, 2013;
77 Barrett & Henley, 2015; Gensini & Allen, 2018; Gensini & Marinaro, 2016; Thompson &
78 Roundy, 2013). While subseasonal forecasts of severe weather have the potential to increase
79 public awareness and preparedness, they could also be beneficial to stakeholders such as
80 emergency managers, catastrophe modelers, and insurance/reinsurance companies (Allen et al.,
81 2016; Gunturi & Tippett, 2017; NOAA/NCEI, 2018; Simmons & Sutter, 2011; Smith &
82 Matthews, 2015). The degree to which subseasonal forecasts could benefit stakeholders was a
83 topic of discussion during the Severe Convection and Climate Workshop held in New York in
84 2016 (Allen et al., 2016). Unsurprisingly, it was concluded that the utility of skillful subseasonal
85 forecasts to the insurance sector would be largely dependent on both their accuracy and having
86 sufficient lead time to impact business decisions involving risk management. For example, if
87 skillful subseasonal forecasts existed, reinsurers would be better equipped to manage the risk of
88 several high-loss severe thunderstorm events occurring in a single season (e.g., the active 2011
89 season) in order to maintain adequate coverage for local insurers and their policyholders. It was
90 also concluded that the scientific understanding of the principal drivers of subseasonal variability
91 could be incorporated by catastrophe modelers and thereby assist insurance companies with their
92 decision making (Allen et al., 2016).

93 Fortunately, to fill the subseasonal “forecast gap,” prior work has identified sources of
94 predictability that have the potential to improve forecasts of severe weather activity in the United
95 States at subseasonal lead times. Two such promising sources of predictability are the Global
96 Wind Oscillation (Gensini & Allen, 2018; Gensini & Marinaro, 2016; Moore, 2017) and the
97 Madden-Julian Oscillation (MJO; Baggett et al., 2017; Barrett & Gensini, 2013; Barrett &
98 Henley, 2015; Kiladis et al., 2014; Matthews, 2008; Mundhenk et al., 2018; Thompson &
99 Roundy, 2013; Wheeler & Hendon, 2004). In this study, we focus on the MJO, which manifests
100 itself in the form of anomalous tropical convection that propagates around the equator with a
101 period of ~30–60 days (Matthews, 2008). Characterized by its amplitude and phase number (1
102 through 8; Kiladis et al., 2014; Wheeler & Hendon, 2004), the MJO is capable of producing
103 Rossby waves that propagate downstream in time and space, thereby influencing the weather at
104 distant extratropical locations over the following several weeks (Baggett et al., 2017; Henderson
105 et al., 2016; Matthews, 2008; Mundhenk et al., 2018; Sardeshmukh & Hoskins, 1988; Zhang,
106 2013). Prior work that has examined the relationship between the MJO and severe weather
107 activity has primarily focused on their contemporaneous, statistical relationship. In other words,
108 previous studies have found that the *current* state of the MJO (its amplitude and phase) has a
109 strong association with the *current* state of severe weather activity over the United States (Barrett
110 & Gensini, 2013; Barrett & Henley, 2015; Thompson & Roundy, 2013). For example, Thompson
111 and Roundy (2013) showed that violent tornado days, that is, 24-hour periods with at least 6
112 tornadoes rated EF2 or greater on the Enhanced Fujita (EF) scale (McDonald & Mehta, 2006),
113 are more frequent when the MJO is in phase 2 than in phase 8.

114 In this study, we build on the foundation of these prior works by hypothesizing that the
115 *current* state of the MJO is a source of predictability and predictive skill for *future* severe

116 weather activity over the United States. To test this hypothesis, we composite environmental
117 parameters associated with severe weather activity, along with tornado and hail events
118 themselves, by MJO phase and lead time (i.e., positive lags) to show that these severe weather
119 phenomena are modulated on weekly timescales by the MJO for several weeks following active
120 MJO phases. Furthermore, we construct a simple empirical prediction model to demonstrate that
121 skillful weekly forecasts of severe weather activity can be made with lead times of 2–5 weeks,
122 using only the current state of the MJO as a predictor.

123

124 **2. Data and Methods**

125 **2.1. Environmental parameters**

126 We derive daily, environmental parameters of surface-based convective available
127 potential energy (CAPE; J kg^{-1}), 0–3-km storm relative helicity (SRH; $\text{m}^2 \text{s}^{-2}$), and their weighted
128 product ($\text{CSRH2} = \text{CAPE} \times \text{SRH}^2$; $\text{m}^6 \text{s}^{-6}$; Lu et al., 2015; Tippett et al., 2012, 2014) from data
129 acquired from the European Centre for Medium-Range Weather Forecasts (ECMWF) interim
130 reanalysis (ERA-Interim; Dee et al., 2011). The data have a horizontal resolution of $1.5^\circ \times 1.5^\circ$
131 and span the years 1979–2015. Daily values of afternoon-averaged CAPE are computed by
132 directly downloading from ERA-Interim, and then averaging, the 6, 9, and 12-hour forecasts
133 from the 1200 UTC reanalysis (i.e., instantaneous 1800, 2100, and 0000 UTC values). Using
134 afternoon-averaged values of CAPE benefits our analysis because it makes it more likely to
135 capture enhanced values of CAPE should they exist on any given afternoon at any given
136 location. Also, while reanalysis-derived CAPE is a forecast product and therefore subject to
137 forecast errors, it has long been shown to be an adequate discriminator of severe thunderstorm
138 environments (e.g., Brooks et al., 2003). Daily values of afternoon-averaged SRH are computed

139 using the Sounding and Hodograph Analysis and Research Program in Python (SHARPPy),
140 which uses the Bunkers' internal dynamics method to calculate the storm-motion vector
141 (Blumberg et al., 2017; Bunkers et al. 2000). As input, SHARPPy is provided 1800 and 0000
142 UTC values of the three-dimensional fields of zonal wind and geopotential from ERA-Interim,
143 along with terrain height. From these values it calculates SRH at the aforementioned synoptic
144 time steps, from which afternoon-averaged values are derived. Daily values of CSRH2 are
145 simply found by multiplying the daily, afternoon-averaged values of CAPE by the square of
146 daily, afternoon-averaged values of SRH. The squaring of SRH is based on Eq. 3 of Tippet et al.
147 (2012) where the best Poisson regression fit between monthly tornado occurrence and
148 environmental parameters across the United States includes an SRH coefficient close to 2.

149

150 **2.2. Tornado and hail events**

151 We obtain daily tornado and hail reports data from the Storm Prediction Center's (SPC)
152 Severe Weather Database (Schaefer & Edwards, 1999). Daily reports of tornadoes with
153 intensities greater than EF1 and hail with diameters greater than 25.4 mm (1 inch) are each
154 aggregated into $1.5^\circ \times 1.5^\circ$ grid boxes, centered on ERA-Interim grid points. We consider a
155 single tornado *event* to have occurred in a given grid box on a particular day if one or more
156 tornado reports occurred therein. In this study, we focus our analysis on regions that subsume 5 x
157 5 grid boxes ($7.5^\circ \times 7.5^\circ$). Thus, by construction, a region can experience between 0 and 25
158 tornado events each day. Similarly, a region can experience 0 and 25 hail events each day. In
159 Text S1, we discuss the sensitivity of our results to the well-documented, non-meteorological
160 heterogeneities that exist in the storm reports data (e.g., Agee & Childs, 2014; Allen & Tippet,
161 2015).

162

163 **2.3. The Madden-Julian Oscillation**

164 The MJO dominates intraseasonal variability in the tropics, manifesting itself as tropical
165 convective and zonal wind anomalies that propagate eastward along the equator with a period of
166 ~30–60 days (Kiladis et al., 2014; Wheeler & Hendon, 2004; Zhang, 2013). Several indices have
167 been developed to describe the current state of the MJO, such as the Real-time Multivariate MJO
168 Index (RMM; Wheeler & Hendon, 2004) and the outgoing longwave radiation (OLR)-based
169 MJO Index (OMI; Kiladis et al., 2014). In this study, we use the OMI and show through
170 supporting figures that our results are generally insensitive to the choice of index. As detailed in
171 (Kiladis et al., 2014), the daily, principal component timeseries (PC1 and PC2) of the OMI are
172 calculated by projecting the 20–96-day band-passed filtered, tropical OLR onto the two leading
173 empirical orthogonal functions of the 30–96-day eastward band-passed filtered, tropical OLR.
174 The MJO is typically characterized by one of eight phases, indicative of where tropical
175 convection is active along the equator, and its amplitude, $\sqrt{(PC1^2 + PC2^2)}$. To maintain
176 geographical consistency with the RMM index, we rotate the OMI by multiplying its PC1 by -1
177 and reverse the order of PC1 and PC2.

178

179 **2.4. Composite analysis**

180 Daily anomalies of CAPE, SRH, CSRH2, tornado events, and hail events are found by
181 subtracting from each variable its smoothed, seasonal cycle. The smoothed, seasonal cycle is
182 found by using Fourier analysis to decompose a given variable's raw, calendar-day climatology
183 into its mean and harmonics. Then, the mean and first two harmonics are summed to construct
184 the smoothed, seasonal cycle. The use of two harmonics captures the secondary peak in severe

185 weather activity that typically occurs during the fall, particularly in the Southeast (e.g., Childs et
186 al., 2018). The composites are constructed by selecting days when the MJO's amplitude is ≥ 1
187 during March–June (MAMJ). For each MJO phase, forward lag composites of consecutive,
188 overlapping weeks (e.g., days +1 through +7, days +2 through +8, and so forth) are made for
189 weekly averaged values of anomalous CAPE, SRH, and CSRH2 and for weekly summed values
190 of anomalous tornado and hail events for their respective $7.5^\circ \times 7.5^\circ$ regions. In keeping with
191 forecasting parlance, we refer to the forward lag dimension of these composites as *lead time*.

192

193 **2.5. The empirical prediction model, its verification, and its skill**

194 Following the methods of (Mundhenk et al., 2018), we create a two-class empirical
195 prediction model to forecast weekly values of either above or below normal CAPE, SRH,
196 CSRH2, tornado events, and hail events at subseasonal lead times for the $7.5^\circ \times 7.5^\circ$ regions
197 described in Sections 2.2 and 2.4. The model incorporates the initial state of the MJO (according
198 to the OMI) as its only predictor. Forecasts are only initialized on days in MAMJ when the
199 OMI's amplitude is ≥ 1 (~61% of all MAMJ days). To generate a forecast, the model compares
200 the median of a variable's conditional distribution (that varies by the initialization date's MJO
201 phase and forecast lead time) to the median of its climatological distribution (that varies only by
202 forecast lead time). Depending on whether the variable's conditional distribution's median is
203 greater than or less than the median of its corresponding climatological distribution, the model
204 predicts above or below normal values of the variable, respectively. We choose to define normal
205 using the median rather than the mean due to the skewness of the distributions associated with
206 tornado and hail events. The distributions are created by drawing samples from the daily
207 anomaly time series of each variable that have been, as in the composites, computed over $7.5^\circ \times$

208 7.5° regions and over consecutive, overlapping weeks (i.e., a 7-day forward running mean). The
209 relevant climatological distribution for a forecast lead time of one week is drawn from March 1
210 through June 30; for a lead time of two weeks, it is drawn from March 8 through July 7. Unlike
211 Mundhenk et al. (2018), we allow the climatological distribution to shift as a function of lead
212 time because of the underlying strong seasonality of the anomalies for each variable.

213 Forecasts for each season are verified independently in a typical leave-one-year-out, cross
214 validation approach (Johnson et al., 2014; Mundhenk et al., 2018). For example, if the model is
215 forecasting for 2015, then the training data to create the forecast derives from 1979–2014 only –
216 meaning all anomalies, their distributions, and their resulting medians are created independently
217 from 2015, the left-out-year. This procedure is repeated 37 times, for each left-out-year. A
218 forecast is verified correct if the observed anomaly in the left-out-year matches the training
219 data’s forecasted anomaly; otherwise the forecast verifies as incorrect.

220 The verification statistics of this two-class empirical prediction model can be segregated
221 into a typical 2×2 contingency table, which we evaluate using the Heidke skill score (HSS;
222 Johnson et al., 2014; Mundhenk et al., 2018; Wilks, 2006). The HSS facilitates a comparison of
223 the empirical prediction model’s skill to that of a climatological reference forecast. Formulated,
224 $HSS = 100 \times (H - E)(T - E)^{-1}$, where H equals the number of correct forecasts, E is the
225 number of correct forecasts expected by chance, and T is the total number of forecasts made.
226 Because the model makes a forecast of above or below normal values with respect to the median
227 of a climatological distribution of that value, it is expected, by chance, to be correct $E = T/2$
228 times (50% of the time). A prediction model that makes correct forecasts all of the time will have
229 an HSS of 100 while one that makes correct forecasts twice as often as incorrect forecasts will
230 have an HSS of 33. A model that makes forecasts with no skill compared to a random forecast

231 receives an HSS of 0, while a model that makes incorrect forecasts more frequently will have a
232 negative HSS.

233

234 **2.6. Statistical significance**

235 Results from the empirical prediction model, and their statistical significance, are
236 presented in Section 5. The null hypothesis we seek to reject in these results can be stated as,
237 “There is no relationship between current, active MJO phases and forecast skill of severe
238 weather variables at extended lead times.” We reject this null hypothesis for certain
239 combinations of MJO phase and lead time through comparing the observed forecast skill to the
240 distribution of skills derived from 1000 random forecast samples. These random forecast
241 samples are generated via a bootstrapping method, with replacement, from the original data.
242 Because the MJO often resides in a particular phase during “blocks” of several days in a row (see
243 Table S1), there is autocorrelation imbedded in the observed forecast that must be reproduced in
244 the random forecast samples. Thus, to reproduce this autocorrelation, we randomize the blocks of
245 days that the MJO is observed to be active. To accomplish this, each of the 566 blocks (sum of
246 the third column in Table S1a) is assigned a random date for the first day of the block (from all
247 MAMJ days during 1979-2015). Then each block is assigned a random MJO phase (1 through
248 8). Having randomized the MJO blocks, the empirical prediction model (as described in Section
249 2.5) is then run, using the randomized MJO blocks on the original data to create a unique random
250 forecast sample. This process is repeated 1000 times to create a distribution of random forecast
251 samples for each combination of MJO phase and lead time. We assign three levels of
252 significance to certain combinations of MJO phase and lead time in the observed forecast has a

253 skill score that exceeds 80%, 90%, and 95% (alpha levels) of the skill scores found in the
254 distribution of random forecast skill scores.

255 The statistical significance presented in Section 4 for the composites is also assessed via a
256 bootstrapping method with 1000 random samples that account for autocorrelation in the observed
257 data. Further details are provided in each figure’s caption.

258

259 **3 Climatology of severe weather variables**

260 Tornadoes and severe hail storms are common across the United States, generating
261 thousands of storm reports annually (Schaefer & Edwards, 1999). In this study, we focus
262 principally on the Plains and the Southeast, two regions heavily impacted by severe weather
263 losses (NOAA/NCEI, 2018); however, we provide results summarizing other regions across the
264 United States in our forthcoming presentations of Figures 3, 4 and 6. In Figure 1, we introduce
265 the spatial and temporal characteristics of the severe weather variables relevant to our study.
266 Figure 1a reveals that most locations east of the Rockies experience ~2 to 4 tornado events per
267 year. In contrast, hail events (Figure 1b) show a distinct preference over the Plains (box
268 delineated in solid white), with frequencies often greater than 12 events per year. Hail events are
269 less common over the Southeast (box delineated in dashed white) where frequencies are
270 generally less than 12 events per year. While some of the noise in these tornado and hail
271 climatologies could be due to the finite duration of the time series we are considering (1979–
272 2015), there are also well-documented, non-meteorological heterogeneities in the data record
273 (e.g., Agee & Childs, 2014; Allen & Tippet, 2015), which we discuss in Text S1.

274 Tornado and hail events over the Plains and Southeast are summed over their
275 corresponding $7.5^\circ \times 7.5^\circ$ regions (25 grid boxes), from which we derive their smoothed

276 seasonal cycles (see Section 2.4). Figures 1c and 1d reveal that tornado and hail events (black
277 and dashed black lines, respectively) peak during March-June (MAMJ; shaded in light brown) in
278 both regions, with events peaking approximately one month earlier in the season over the
279 Southeast. Severe thunderstorms are most common during MAMJ because the large-scale
280 environmental conditions most favorable for their development – namely, instability, high
281 vertical wind shear, and convective initiation mechanisms (e.g., drylines, frontal passages, and
282 short wave troughs) – are most likely to be realized together at this time of year (Tippett et al.,
283 2015). Initiation mechanisms are difficult to quantify (Tippett et al., 2015) and thus will only be
284 analyzed from a large-scale perspective of how 500-hPa height anomalies promote surface-level
285 patterns favorable to convective initiation and how these height anomalies are modified by the
286 MJO. We focus more intensely on CAPE and SRH, common measures of instability and
287 directional wind shear, respectively (e.g., Allen et al., 2015a; Barrett & Gensini, 2013; Barrett &
288 Henley, 2015; Brooks et al., 2003; Gensini & Ashley, 2011; Tippett, 2014; Tippett et al., 2012,
289 2014, 2015). Also, we examine a combined environmental parameter, CSRH2, because it
290 exhibits higher covariance with tornado and hail reports than either CAPE or SRH alone (Lu et
291 al., 2015; Tippett et al., 2012, 2014). In fact, Figures 1c and 1d provide evidence that CSRH2
292 (violet line) serves as a reasonable proxy to tornado and hail events for both the Plains and the
293 Southeast, as the peak in the seasonal cycle of CSRH2 is more aligned with them compared to
294 either CAPE (red line) or SRH (blue line). It is certainly possible that combined environmental
295 parameters other than CSRH2 have better empirical fits with tornado and hail events, particularly
296 when location and time of year are considered (e.g., Allen et al., 2015a; Rasmussen et al. 1998,
297 Tippett et al., 2014, 2015). However, an exhaustive examination of these environmental
298 parameters is not the principal focus of our study. Rather, our findings involving CAPE, SRH,

299 and CSRH2 are simply meant to lend support to our findings related to actual tornado and hail
300 events.

301

302 **4 Subseasonal modulation by the MJO**

303 Figure 2 displays composites of weekly averaged values of anomalous CAPE, SRH, and
304 CSRH2 along with weekly summed values of anomalous tornado and hail events. Each
305 composite is presented as a function of MJO phase and lead time for both the Plains and the
306 Southeast. At zero lead times, we observe modulation of the severe weather variables by MJO
307 phase that qualitatively agree with prior studies (Barrett & Gensini, 2013; Barrett & Henley,
308 2015; Thompson & Roundy, 2013). For example, as in Thompson and Roundy (2013), we
309 observe at short lead times a higher frequency of tornado events when the MJO is in phase 2 in
310 contrast to phase 8 when we observe lower frequencies (Figures 2d and 2i). However, what is
311 novel here is the clear propagating signal of the anomalies through MJO phase and lead time
312 space that extends to subseasonal lead times of 2–5 weeks – not only of the environmental
313 parameters, but of the tornado and hail events themselves. These anomalies often approach
314 deviations of ~30% from their climatological March–July values. Moreover, the magnitudes of
315 the anomalies generally do not weaken with lead time and in fact show signs of strengthening at
316 lead times of 2–3 weeks. This behavior is consistent with the ~10–14 days that Rossby waves
317 take to travel from the tropics and influence the United States (Sardeshmukh & Hoskins, 1988;
318 Zhang, 2013). Also, the observed propagation through MJO phase and lead time space is
319 consistent with the period of a typical MJO of ~30–60 days (Kiladis et al., 2014; Matthews,
320 2008; Wheeler & Hendon, 2004). For example, in Figure 2a, the highest values of anomalous

321 CAPE reside in each MJO phase for ~5 days, transitioning from occurring immediately
322 following phase 4 to ~20 days following phase 1.

323 We wish to note that we purposely do not show statistical significance in our presentation
324 of Figure 2. Instead, we wish to emphasize the clear propagating signal through MJO phase and
325 lead time space that extends through the composites rather than focus on the significance of any
326 particular grid point. It can be reasonably surmised that these propagating signals do not happen
327 by chance. Nevertheless, to see statistical significance, we reproduce Figure 2 in Figure S1. As
328 expected, the largest anomalies along the propagating signals through MJO phase and lead time
329 space are significant, particularly in the Plains (Figures S1a to S1e). While grid point by grid
330 point significance is less over the Southeast, the propagating signals are still present which lends
331 confidence that there is a dynamical link to the MJO (e.g., SRH and tornado events in Figure S1g
332 and S1i, respectively).

333 Returning to our discussion of Figure 2, we note that not only are the environmental
334 parameters of CAPE, SRH, and CSRH2 modulated by the MJO at extended lead times, the actual
335 tornado and hail events are as well (Figures 2d, 2e, 2i, and 2j). In particular, the tornado and hail
336 events in the Plains have propagating signals through MJO phase and lead time space entirely
337 consistent with those of the aforementioned parameters. Pattern correlations calculated across
338 MJO phase and lead time space between the composites of tornado events with those of CAPE,
339 SRH, and CSRH2 in the Plains are 0.58, 0.59, and 0.72, respectively. For hail events, the values
340 are 0.68, 0.54, and 0.73. Each value is significant at the 95% confidence level. While the pattern
341 correlations in the Plains reveal that CSRH2 is a better proxy for tornado and hail events than
342 CAPE or SRH alone, this is supported even more in the Southeast. There, tornado events have
343 pattern correlations of -0.29, 0.68, and 0.76 with CAPE, SRH, and CSRH2, respectively. For hail

344 events, the values are 0.13, 0.27, and 0.39. The pattern correlations involving CAPE are not
345 significant at the 95% confidence level, but those involving CSRH2 are. As illustrated in Figure
346 3, the aforementioned pattern correlations associated with the Plains and Southeast regions
347 (highlighted by the black open circles that represent the centers of these 7.5° by 7.5° regions) are
348 representative of the pattern correlations associated with their neighboring regions. These pattern
349 correlations are derived from the composites (not shown) of overlapping $7.5^\circ \times 7.5^\circ$ regions,
350 centered every 1.5° in longitude from 258.0°E to 282.0°E and every 1.5° in latitude from 28.5°N
351 to 45.0°N . This analysis illustrates the utility of a combined parameter, such as CSRH2, in
352 diagnosing environments favorable to severe weather at subseasonal timescales, as the relative
353 importance of CAPE and SRH differ by region and by season. For example, CAPE exhibits
354 negative pattern correlations with tornado events for regions over the southeastern United States
355 during MAMJ (Figure 3a) while SRH (Figure 3c) and CSRH2 (Figure 3e) have significantly
356 positive pattern correlations during this period. Indeed, it has been shown that kinematic
357 parameters such as SRH can be more useful as a severe weather discriminator than
358 thermodynamic parameters, such as CAPE (Grams et al., 2012; Tippett et al., 2015).
359 Furthermore, there exists a propensity for high-shear, low-CAPE severe weather environments in
360 the Southeast, due in part to lower lapse rates, as compared to the Plains (Sherburn & Parker,
361 2014).

362 It is useful to examine how 500-hPa height anomalies vary by MJO phase and lead time
363 (Figure 4) in order to physically explain the observed modulation of the environmental
364 parameters of CAPE, SRH, and CSRH2. Moreover, an examination of 500-hPa height anomalies
365 can also reveal some plausible convective initiation mechanisms. Because the MJO induces
366 Rossby waves that propagate into the mid-latitudes, it is capable of modulating the 500-hPa

367 height patterns over the United States (Baggett et al., 2017; Henderson et al., 2016; Mundhenk et
368 al., 2018; Sardeshmukh & Hoskins, 1988; Zhang, 2013). The composites in Figure 4 reveal that
369 significant modulation of the 500-hPa heights, taking the form of anomalous troughs and ridges,
370 exists for most MJO phases and lead weeks. In fact, upon closer inspection, these anomalous
371 troughs and ridges propagate across MJO phase and lead week in a manner consistent with the
372 ~30–60 day period of a typical MJO. For example, the anomalous ridge in the eastern United
373 States that exists during the first week following phase 4 transitions to occurring in the third
374 week following phase 2. Similarly, the anomalous trough in the eastern United States that exists
375 during the first week following phase 8 transitions to occurring in the fifth week following phase
376 3. The location of the troughs and ridges are physically important because they help explain the
377 observed modulation of the severe weather variables displayed in Figure 2. At a basic level, a
378 favorable height pattern in the Plains for severe weather consists of an anomalous ridge over the
379 eastern United States paired with a trough to the west (e.g., during week 2 following phase 3 in
380 Figure 4). Consistent with Figure 2a, this pattern enhances CAPE by inducing anomalous
381 moisture transport out of the Gulf of Mexico (as indicated by the black vectors which represent
382 vertically integrated vapor transport). Also consistent with Figure 2b, this pattern provides
383 support for convective initiation and organization as any short wave troughs or cold fronts that
384 rotate through the trough can provide upper-level divergence, synoptic-scale upward vertical
385 motion, and vertical shear, as expected from quasi-geostrophic theory (Eady, 1949).

386 To conclude this section, we note that in some respects, it is surprising to see the
387 modulation of 500-hPa heights and severe weather variables at such extended lead times across
388 all MJO phases during MAMJ. Some prior studies have shown that the MJO's ability to generate
389 Rossby waves is dependent on the phase of the MJO, that Rossby wave generation is most

390 prominent during boreal winter, that these Rossby waves only exist for ~15 days, and that the
391 teleconnections produced by these Rossby waves can vary at monthly timescales (e.g., Barrett &
392 Henley, 2015; Cassou 2008; Seo & Son 2012). To reconcile these studies with our own, it is
393 important to consider that the MJO has a typical propagation period of ~30–60 days. Therefore,
394 if a particular phase of the MJO physically forces a teleconnection, then that same teleconnection
395 may appear in our composites for other phases of the MJO without actually being forced by
396 those phases. However, because the MJO typically exhibits a semi-coherent progression through
397 sequential phases (Matthews 2008), the teleconnection will appear at different lead times in our
398 composites – longer lead times for phases prior to the phase responsible for the forcing and
399 shorter lead times for phases following the phase responsible for the forcing. Propagating
400 teleconnections through MJO phase and lead time space are highlighted in our earlier discussions
401 of Figures 2 and 4. Also, while most studies have focused on the MJO’s influence during boreal
402 winter, this does not preclude the MJO having a substantial influence during MAMJ. While our
403 study and others (Barrett & Gensini, 2013; Barrett & Henley, 2015; Thompson & Roundy, 2013)
404 demonstrate a statistical connection between the MJO and severe weather over the United States
405 during MAMJ, studies with a more dynamical focus, such as idealized model simulations, would
406 be worthwhile.

407

408 **5 Skillful subseasonal forecasts using the MJO**

409 The composites in Figure 2 offer compelling evidence that the MJO modulates severe
410 weather activity over the Plains and Southeast at subseasonal lead times. Therefore, a natural
411 question to ask is whether the MJO is in fact a source of predictive skill – in other words, can we
412 skillfully forecast severe weather activity at subseasonal lead times with knowledge of the

413 current MJO state? To answer this question, we employ the empirical prediction model
414 (explained in detail in Section 2.5) to issue forecasts for consecutive, overlapping weeks with
415 forecast leads of 1–29 days after the day the forecast is issued. It is important to emphasize here
416 that forecasts are not being made to predict the occurrence of a specific severe thunderstorm on a
417 particular day at a precise location. Rather, the forecasts are issued for above or below normal
418 activity in broad $7.5^\circ \times 7.5^\circ$ regions over weekly time scales.

419 Figure 5 presents the skill scores of the empirical prediction model for forecasts of
420 CAPE, SRH, CSRH2, tornado events, and hail events for both the Plains and the Southeast.
421 Shaded regions indicate where the model has positive skill and thus, is more skillful than an
422 equal-chances, random forecast. Warm and cool colors denote when above or below normal
423 activity is forecast, respectively. In a manner consistent with the composites (Figure 2), positive
424 skill scores propagate through MJO phase and lead time space for each environmental parameter
425 in both the Plains and the Southeast (Figures 5a-5c and 5f-5h). Moreover, for the Plains, we see
426 significantly positive, propagating skill scores for actual tornado and hail events (Figures 5d and
427 5e). Generally, the highest skill scores are collocated with the highest anomalies in the
428 composites (compare Figures 2 and 5). Some of these high skill scores have values approaching
429 33, which implies a 2:1 ratio of correct to incorrect forecasts, a significant improvement over an
430 equal-chances, random forecast. Most importantly, these significantly positive skill scores extend
431 to forecast lead times of 2–5 weeks, well into subseasonal timescales. These forecast lead times
432 for environmental parameters favorable to severe weather activity represent a significant
433 improvement over the mid-latitude predictability barrier of ~ 14 days that currently exists in
434 state-of-the-art, numerical weather models (Baggett et al., 2017; Carbin et al., 2016; Vitart,
435 2017). Furthermore, the forecast lead times on display for actual tornado and hail events in the

436 Plains offer an opportunity to extend short-term, daily outlooks (such as those issued by SPC) to
437 subseasonal, weekly outlooks.

438 We test the robustness of our prediction model by performing a leave-three-years-out
439 cross validation approach. Overall we find our results to be qualitatively insensitive to using a
440 leave-three-years-out versus a leave-one-year-out cross validation approach (compare Figures 5
441 and S2). Moreover, our results are qualitatively insensitive to the choice of MJO index (compare
442 Figures 2 and 5 to Figures S3 and S4, respectively), although skill scores are generally higher
443 using the OMI rather than the RMM index. We hypothesize that this difference in skill scores
444 results from the OMI being more directly analogous to OLR (and by extension, tropical
445 convection, Rossby wave source dynamics, and mid-latitude teleconnections) than the RMM,
446 which also incorporates equatorial zonal winds (Kiladis et al., 2014; Sardeshmukh & Hoskins,
447 1988; Wheeler & Hendon, 2004). Testing of this hypothesis is beyond the scope of our study.

448 The combinations of MJO phase and forecast lead time that have significantly positive
449 skill scores should be considered “forecasts of opportunity” because there are many other
450 combinations that have very small positive or negative skill scores (white shading in Figure 5).
451 Thus, a forecaster would need to be opportunistic in issuing forecasts when they have a higher
452 probability of success. Moreover, the combinations of MJO phase and forecast lead time that
453 have significantly positive skill scores vary by region. This is particularly true when comparing
454 the relatively high skill scores of the forecasts generated for tornado and hail events in the Plains
455 to those in the Southeast, where little skill is observed (compare Figures 5d and 5e to Figures 5i
456 and 5j, respectively). In fact, when the skill scores are averaged over MJO phase and lead time
457 space for each overlapping $7.5^\circ \times 7.5^\circ$ region (Figure 6), it becomes quickly apparent that
458 regions located in the Plains consistently exhibit higher average skill scores for each severe

459 weather variable than other regions, while regions located in the South have relatively lower
460 average skill scores for each variable except SRH (Figure 6b). Interestingly, with respect to
461 SRH, there is a band of lower average skill scores running from the Central Plains through the
462 Ohio River Valley, suggesting that the underlying variability of the jet stream for a given MJO
463 phase has a more negative impact on predictability there than elsewhere. While understanding
464 the root cause of these different average skill scores across regions is beyond the current scope of
465 this study, it is important to emphasize that forecasts of opportunity exist in most regions, and
466 that these forecasts of opportunity vary by MJO phase and forecast lead time. For example, if a
467 forecaster wishes to issue guidance for tornado activity at a lead time of 4 weeks (Figure 5d),
468 then he or she should have confidence in above normal activity in the Plains if the MJO were
469 currently in phases 7 or 8.

470

471 **6 Conclusion and discussion**

472 Using only the current phase of an active MJO as a predictor, we have constructed a
473 simple two-class empirical model that provides skillful subseasonal forecasts for several large-
474 scale environmental parameters associated with severe weather activity, namely CAPE, SRH,
475 and CSRH2. Moreover, we have demonstrated skillful forecasts of actual tornado and hail events
476 in certain regions, such as the Plains, with lead times extending out to 5 weeks. While the
477 principal question we set out to answer in this study revolved around the ability of the MJO to
478 serve as a source of predictive skill, the simplicity of the two-class empirical model we
479 developed lends opportunity to the addition of more predictors and additional classes that could
480 lead to its improvement. Some potential predictors that operate on subseasonal and longer time
481 scales include ENSO (Allen et al., 2015b; Childs et al., 2018; Cook et al., 2017; Lepore et al.,

482 2017), the Global Wind Oscillation (Gensini & Allen, 2018; Gensini & Marinaro, 2016; Moore,
483 2017), Gulf of Mexico sea surface temperatures (Molina et al., 2016), antecedent drought
484 conditions (Shepherd et al., 2009), the quasi-biennial oscillation (Baggett et al., 2017; Mundhenk
485 et al., 2018; Son et al., 2017), the Arctic oscillation (Childs et al., 2018), and decadal-scale trends
486 (Diffenbaugh et al., 2013; Tippett, 2014). ENSO has been shown to be a skillful predictor of
487 severe weather activity at seasonal time scales (Allen et al., 2015b; Lepore et al., 2017). Thus, an
488 empirical prediction model that uses both ENSO and the MJO as predictors (e.g., Slade &
489 Maloney, 2013) may provide additional skill by capturing the subseasonal modulation of severe
490 weather activity by the MJO juxtaposed onto the interannual modulation by ENSO. With respect
491 to the quasi-biennial oscillation, recent work has shown that it impacts the amplitude of the MJO
492 and therefore the MJO's impact on weather downstream (Baggett et al., 2017; Mundhenk et al.,
493 2018; Son et al., 2017). Further, the Arctic oscillation, whose influence is most realized during
494 winter and spring over the eastern United States, may be particularly useful in improving skill
495 scores in the Southeast (Childs et al., 2018), where severe weather peaks earlier in the year
496 (Figures 1c and 1d).

497 Numerical weather models also offer hope in improving predictions of environmental
498 parameters favorable to severe weather activity. Individual model runs of the Climate Forecast
499 System, version 2 (CFSv2) generally show skill in predicting such environments with lead times
500 of ~7 days (Carbin et al., 2016). However, Carbin et al. (2016) demonstrated that the possibility
501 exists to extend these skillful lead times by several weeks through a lagged ensemble approach
502 whereby consecutive model runs serve as an ensemble prediction for the same forecast
503 verification date. Development of an empirical prediction model that uses both the lagged
504 ensemble approach and the MJO as predictors could prove a useful venture to that end. With

505 respect to the MJO, numerical models are increasingly skillful at predicting its propagation along
506 the equator, with skillful lead times of 4–5 weeks realized by the European Centre for Medium-
507 Range Weather Forecast (ECMWF) model (Kim et al., 2016; Vitart, 2017). It is conceivable that
508 the skillful lead times of an empirical model can be extended by initializing it with a numerical
509 model’s forecasted state of the MJO. Regardless of how our empirical model’s skill is eventually
510 improved, our results show that knowledge of the MJO is an important source of predictability
511 *and* prediction skill of tornado and severe hail events for certain weeks and regions at lead times
512 of 2–5 weeks. While it remains to be seen if the forewarning provided by the MJO is actionable
513 in real-time by emergency managers and stakeholders to protect lives and property, these results
514 nonetheless represent an important scientific advancement in our understanding of an important
515 source of subseasonal predictability of severe weather.

516

517 **Acknowledgments**

518 This research has been conducted as part of the NOAA MAPP S2S Prediction Task Force and
519 supported by NOAA grant NA16OAR4310064. Additional support was received from NSF
520 Climate and Large-scale Dynamics Program grant AGS-1441916, NWS grant
521 NA16NWS4680022, NSF Graduate Research Fellowship Program grant DGE-1321845, NSF
522 REU Site in Climate Science at CSU grant AGS-1461270, and a sub-award under the FIRO
523 project at CW3. We thank Michael K. Tippett for fostering dialogue and five anonymous
524 reviewers who have all helped to improve the manuscript. All coding was performed in the
525 National Center for Atmospheric Research Command Language (NCL) version V.6.4.0, Python
526 V.2.7.12, the Sounding and Hodograph Analysis and Research Program in Python (SHARPy)

527 V.1.3.0, and Matlab V.R2015b. Access information to all data repositories is provided in Text
528 S2.

529 **References**

- 530 Agee, E., & Childs, S. (2014). Adjustments in tornado counts, F-scale intensity, and path width
531 for assessing significant tornado destruction. *Journal of Applied Meteorology and*
532 *Climatology*, 53(6), 1494-1505. <https://doi.org/10.1175/jamc-d-13-0235.1>
- 533 Allen, J. T., & Tippet, M. K. (2015). The characteristics of United States hail reports: 1955-2014,
534 *Electronic Journal Severe Storms Meteorology*, 10, 1-31.
- 535 Allen, J. T., Tippet, M. K., & Sobel, A. H. (2015a). An empirical model relating U.S. monthly
536 hail occurrence to large-scale meteorological environment. *Journal of Advances in*
537 *Modeling Earth Systems*, 7(1), 226-243. <https://doi.org/10.1002/2014ms000397>
- 538 Allen, J. T., Tippet, M. K., & Sobel, A. H. (2015b). Influence of the El Nino/Southern
539 Oscillation on tornado and hail frequency in the United States. *Nature Geoscience*, 8(4),
540 278-283. <https://doi.org/10.1038/Ngeo2385>
- 541 Allen, J. T., Tippet, M. K., Sobel, A. H., & Lepore, C. (2016). Understanding the drivers of
542 variability in severe convection: Bringing together the scientific and insurance
543 communities. *Bulletin of the American Meteorological Society*, 97(11), ES221-ES223.
544 <https://doi.org/10.1175/bams-d-16-0208.1>
- 545 Baggett, C. F., Barnes, E. A., Maloney, E. D., & Mundhenk, B. D. (2017). Advancing
546 atmospheric river forecasts into subseasonal-to-seasonal timescales. *Geophysical*
547 *Research Letters*, 44(14), 7528-7536. <https://doi.org/10.1002/2017gl074434>
- 548 Barrett, B. S., & Gensini, V. A. (2013). Variability of central United States April-May tornado
549 day likelihood by phase of the Madden-Julian Oscillation. *Geophysical Research Letters*,
550 40(11), 2790-2795. <https://doi.org/10.1002/grl.50522>

- 551 Barrett, B. S., & Henley, B. N. (2015). Intraseasonal variability of hail in the contiguous United
552 States: Relationship to the Madden-Julian Oscillation. *Monthly Weather Review*, 143(4),
553 1086-1103. <https://doi.org/10.1175/Mwr-D-14-00257.1>
- 554 Blumberg, W. G., Halbert, K. T., Supinie, T. A., Marsh, P. T., Thompson, R. L., & Hart, J. A.
555 (2017). SHARPPy: An open-source sounding analysis toolkit for the atmospheric
556 sciences. *Bulletin of the American Meteorological Society*, *98*(8), 1625-1636.
557 <https://doi.org/10.1175/bams-d-15-00309.1>
- 558 Bunkers, M. J., Klimowski, B. A., Zeitler, J. W., Thompson, R. L., & Weisman, M. L. (2000).
559 Predicting supercell motion using a new hodograph technique. *Weather and Forecasting*,
560 *15*, 61-79. [https://doi.org/10.1175/1520-0434\(2000\)015<0061:PSMUAN>2.0.CO;2](https://doi.org/10.1175/1520-0434(2000)015<0061:PSMUAN>2.0.CO;2)
- 561 Brooks, H. E., Lee, J. W., & Craven, J. P. (2003). The spatial distribution of severe thunderstorm
562 and tornado environments from global reanalysis data. *Atmospheric Research*, *67-68*, 73-
563 94. [https://doi.org/10.1016/s0169-8095\(03\)00045-0](https://doi.org/10.1016/s0169-8095(03)00045-0)
- 564 Cassou, C. (2008). Intraseasonal interaction between the Madden-Julian Oscillation and the North
565 Atlantic Oscillation. *Nature*, *455*(7212), 523-527. <https://doi.org/10.1038/nature07286>
- 566 Carbin, G. W., Tippett, M. K., Lillo, S. P., and Brooks, H. E. (2016). Visualizing long-range
567 severe thunderstorm environment guidance from CFSv2. *Bulletin of the American*
568 *Meteorological Society*, *97*(6), 1021-1031. <https://doi.org/10.1175/bams-d-14-00136.1>
- 569 Childs, S. J., Schumacher, R. S., & Allen, J. T. (2018). Cold-season tornadoes: Climatological
570 and meteorological insights. *Weather and Forecasting*, *33*(3), 671-691.
571 <https://doi.org/10.1175/waf-d-17-0120.1>
- 572 Cook, A. R., Leslie, L. M., Parsons, D. B., & Schaefer, J. T. (2017). The impact of El Niño–
573 Southern Oscillation (ENSO) on winter and early spring U.S. tornado outbreaks. *Journal*

- 574 *of Applied Meteorology and Climatology*, 56(9), 2455-2478.
575 <https://doi.org/10.1175/jamc-d-16-0249.1>
- 576 Dee, D. P., et al. (2011). The ERA-Interim reanalysis: configuration and performance of the data
577 assimilation system. *Quarterly Journal of the Royal Meteorological Society*, 137(656),
578 553-597. <https://doi.org/10.1002/qj.828>
- 579 Diffenbaugh, N. S., Scherer, M., & Trapp, R. J. (2013). Robust increases in severe thunderstorm
580 environments in response to greenhouse forcing. *Proceedings of the National Academy of*
581 *the Sciences*, 110(41), 16361-16366. <https://doi.org/10.1073/pnas.1307758110>
- 582 Eady, E. T. (1949). Long waves and cyclone waves. *Tellus*, 1(3), 33-52.
583 <https://doi.org/10.1111/j.2153-3490.1949.tb01265.x>
- 584 Gensini, V. A., & Ashley, W. S. (2011). Climatology of potentially severe convective
585 environments from North American regional reanalysis. *Electronic Journal Severe*
586 *Storms Meteorology*, 6(8), 1-40.
- 587 Gensini, V. A., & Marinaro, A. (2016). Tornado frequency in the United States related to global
588 relative angular momentum. *Monthly Weather Review*, 144(2), 801-810.
589 <https://doi.org/10.1175/mwr-d-15-0289.1>
- 590 Gensini, V. A., & Allen, J. T. (2018). United States hail frequency and the global wind
591 oscillation. *Geophysical Research Letters*, 45(3), 1611-1620.
592 <https://doi.org/10.1002/2017gl076822>
- 593 Grams, J. S., R. L. Thompson, D. V. Snively, J. A. Prentice, G. M. Hodges, and L. J. Reames,
594 2012: A Climatology and Comparison of Parameters for Significant Tornado Events in
595 the United States. *Weather and Forecasting*, 27, 106-123. [https://doi.org/10.1175/waf-](https://doi.org/10.1175/waf-d-11-00008.1)
596 [d-11-00008.1](https://doi.org/10.1175/waf-d-11-00008.1)

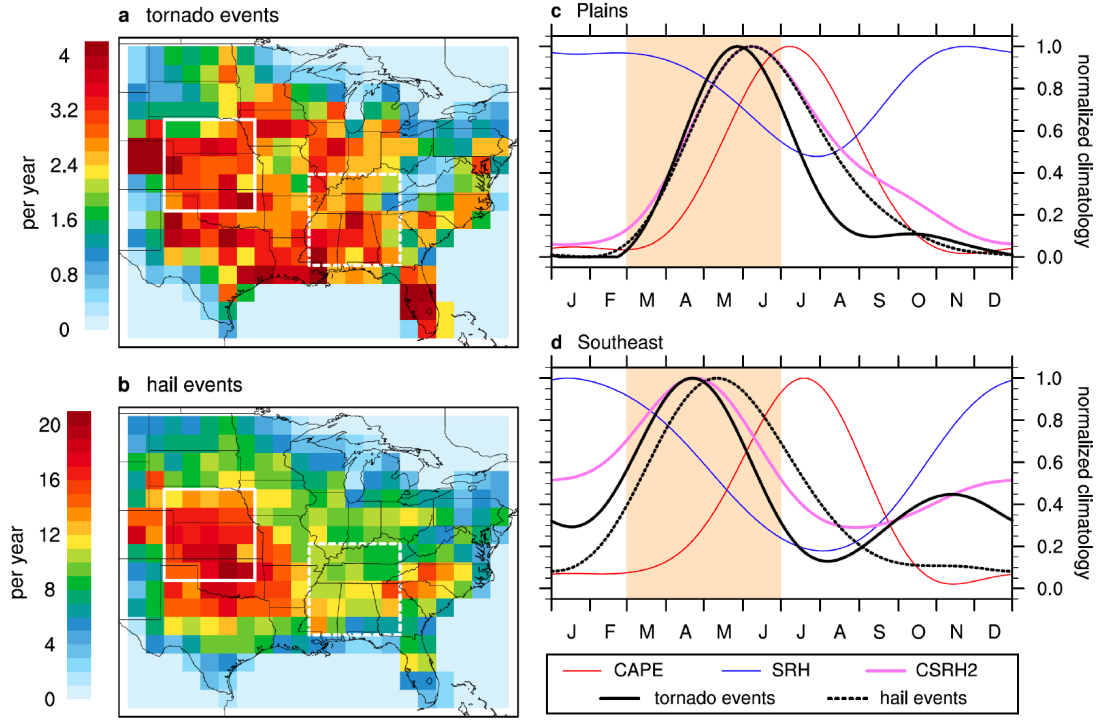
- 597 Gunturi, P., & Tippett, M. K. (2017). Impact of ENSO on U.S. tornado and hail frequencies.
598 *Managing Severe Thunderstorm Risk*, Technical Report, WillisRe.
- 599 Henderson, S. A., Maloney, E. D., & Barnes, E. A. (2016). The influence of the Madden-Julian
600 Oscillation on Northern Hemisphere winter blocking. *Journal of Climate*, 29(12), 4597-
601 4616. <https://doi.org/10.1175/Jcli-D-15-0502.1>
- 602 Herman, G. R., Nielsen, E. R., & Schumacher, R. S. (2017). Probabilistic verification of Storm
603 Prediction Center convective outlooks. *Weather and Forecasting*, 33(1), 161-184.
604 <https://doi.org/10.1175/waf-d-17-0104.1>
- 605 Johnson, N. C., Collins, D. C., Feldstein, S. B., L'Heureux, M. L., & Riddle, E. E. (2014).
606 Skillful wintertime North American temperature forecasts out to 4 weeks based on the
607 state of ENSO and the MJO*. *Weather and Forecasting*, 29(1), 23-38.
608 <https://doi.org/10.1175/waf-d-13-00102.1>
- 609 Kiladis, G. N., Dias, J. , Straub, K. H., Wheeler, M. C., Tulich, S. N., Kikuchi, K., Weickmann,
610 K. M., & Ventrice, M. J. (2014). A comparison of OLR and circulation-based indices for
611 tracking the MJO. *Monthly Weather Review*, 142(5), 1697-1715.
612 <https://doi.org/10.1175/Mwr-D-13-00301.1>
- 613 Kim, H. M., Kim, D., Vitart, F., Toma, V. E., Kug, J. S., & Webster, P. J. (2016). MJO
614 propagation across the Maritime Continent in the ECMWF Ensemble Prediction System.
615 *Journal of Climate*, 29(11), 3973-3988. <https://doi.org/10.1175/Jcli-D-15-0862.1>
- 616 Lepore, C., Tippett, M. K., & Allen, J. T. (2017). ENSO-based probabilistic forecasts of March-
617 May U.S. tornado and hail activity. *Geophysical Research Letters*, 44(17), 9093-9101.
618 <https://doi.org/10.1002/2017gl074781>

- 619 Lu, M., Tippett, M. K., & Lall, U. (2015). Changes in the seasonality of tornado and favorable
620 genesis conditions in the central United States. *Geophysical Research Letters*, *42*(10),
621 4224-4231. <https://doi.org/10.1002/2015gl063968>
- 622 Matthews, A. J. (2008). Primary and successive events in the Madden–Julian Oscillation.
623 *Quarterly Journal of the Royal Meteorological Society*, *134*(631), 439-453.
624 <https://doi.org/10.1002/qj.224>
- 625 McDonald, J. R., & Mehta, K. C. (2006). A recommendation for an Enhanced Fujita Scale (EF-
626 Scale). Technical Report, Texas Tech University: Wind Science and Engineering Center.
- 627 Molina, M. J., Timmer, R. P., & Allen, J. T., (2016). Importance of the Gulf of Mexico as a
628 climate driver for U.S. severe thunderstorm activity. *Geophysical Research Letters*,
629 *43*(23), 12,295-12,304. <https://doi.org/10.1002/2016gl071603>
- 630 Moore, T. W. (2017). Annual and seasonal tornado activity in the United States and the global
631 wind oscillation. *Climate Dynamics*, *50*(11-12), 4323-4334.
632 <https://doi.org/10.1007/s00382-017-3877-5>
- 633 Mundhenk, B. D., Barnes, E. A., Maloney, E. D., & Baggett, C. F. (2018). Skillful empirical
634 subseasonal prediction of landfalling atmospheric river activity using the Madden–Julian
635 oscillation and quasi-biennial oscillation. *npj Climate and Atmospheric Science*, *1*(1), 1-7.
636 <https://doi.org/10.1038/s41612-017-0008-2>
- 637 NOAA Storm Prediction Center (SPC) (2018). *SPC Products*. Retrieved from
638 <https://www.spc.noaa.gov/misc/about.html>.
- 639 NOAA National Centers for Environmental Information (NCEI) (2018). *U.S. Billion-Dollar*
640 *Weather and Climate Disasters*. Retrieved from <https://www.ncdc.noaa.gov/billions/>.

- 641 Rasmussen, E. N., & Blanford, D. O., (1998). A baseline climatology of sounding-derived
642 supercell and tornado forecast parameters. *Weather and Forecasting*, *13*, 1148-1164,
643 [https://doi.org/10.1175/1520-0434\(1998\)013<1148:Abcosd>2.0.Co;2](https://doi.org/10.1175/1520-0434(1998)013<1148:Abcosd>2.0.Co;2)
- 644 Sardeshmukh, P. D., & Hoskins, B. J. (1988). The generation of global rotational flow by steady
645 idealized tropical divergence. *Journal of Atmospheric Sciences*, *45*(7), 1228-1251.
646 [https://doi.org/10.1175/1520-0469\(1988\)045<1228:Tgogrf>2.0.Co;2](https://doi.org/10.1175/1520-0469(1988)045<1228:Tgogrf>2.0.Co;2)
- 647 Seo, K. H., & Son, S. W. (2012). The global atmospheric circulation response to diabatic heating
648 associated with the Madden-Julian Oscillation during northern winter. *Journal of the*
649 *Atmospheric Sciences*, *69*(1), 79-96. <https://doi.org/10.1175/2011jas3686.1>
- 650 Schaefer, J. T., & Edwards, R. (1999). The SPC Tornado/Severe Thunderstorm Database. *In*
651 *Preprints, 11th Conference of Applied Meteorology*. (pp. 215-220). Dallas TX: American
652 Meteorological Society.
- 653 Shepherd, M., Niyogi, D., & Mote, T. L. (2009). A seasonal-scale climatological analysis
654 correlating spring tornadic activity with antecedent fall–winter drought in the
655 southeastern United States. *Environmental Research Letters*, *4*(2), 1-7.
656 <https://doi.org/10.1088/1748-9326/4/2/024012>
- 657 Sherburn, K. D., Parker, M. D. (2014). Climatology and ingredients of significant severe
658 convection in high-shear, low-CAPE environments. *Weather and Forecasting*, *29*(4),
659 854-877. <https://doi.org/10.1175/waf-d-13-00041.1>
- 660 Simmons, K., & Sutter, D. (2011). *Economic and societal impacts of tornadoes, U.S.A.:*
661 American Meteorological Society.

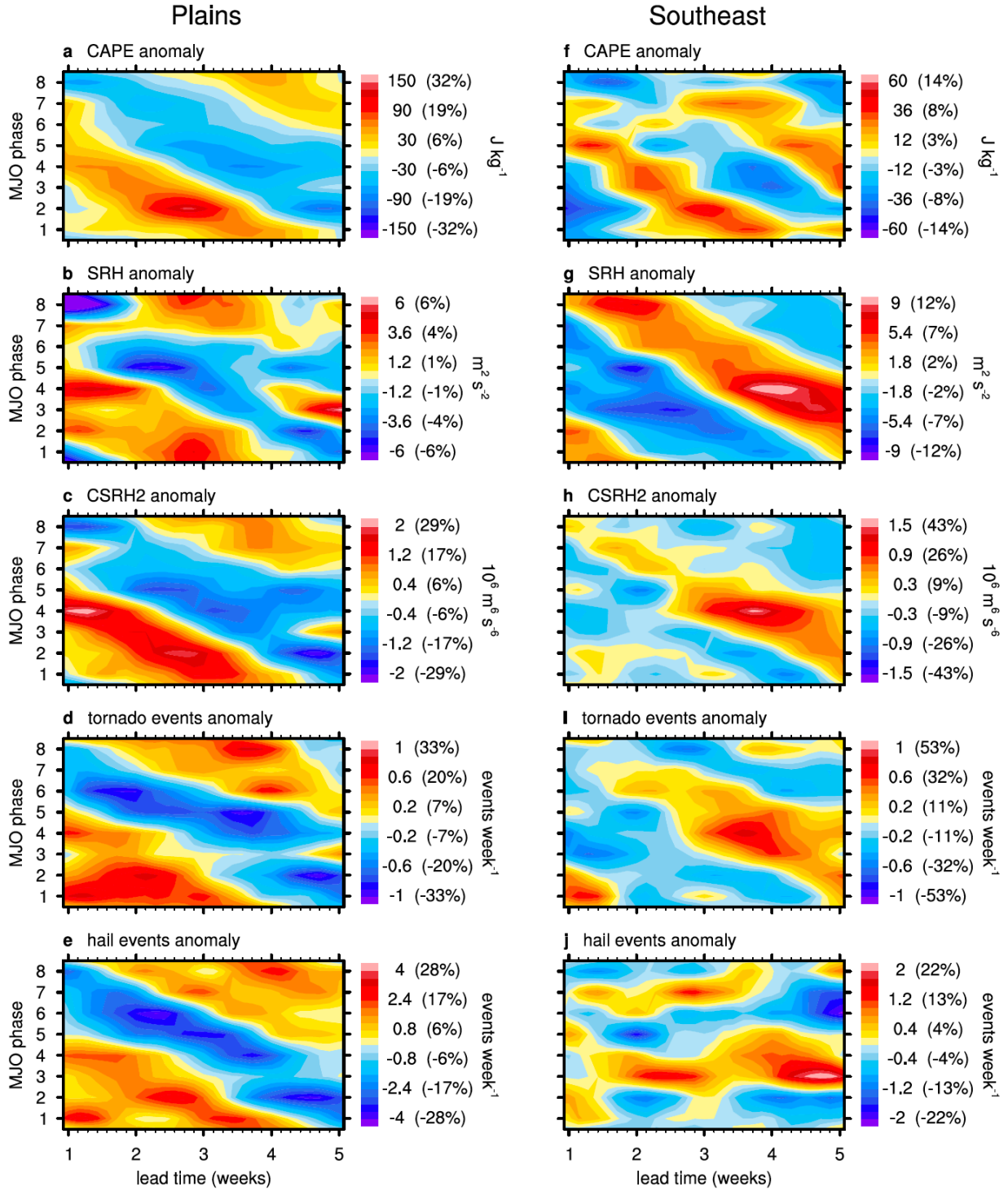
- 662 Slade, S. A., & Maloney, E. D. (2013). An intraseasonal prediction model of Atlantic and East
663 Pacific tropical cyclone genesis. *Monthly Weather Review*, *141*(6), 1925-1942.
664 <https://doi.org/10.1175/mwr-d-12-00268.1>
- 665 Smith, A. B., & Matthews, J. L. (2015). Quantifying uncertainty and variable sensitivity within
666 the US billion-dollar weather and climate disaster cost estimates. *Natural Hazards*, *77*(3),
667 1829-1851. <https://doi.org/10.1007/s11069-015-1678-x>
- 668 Son, S. W., Lim, Y., Yoo, C., Hendon, H. H., & Kim, J. (2017). Stratospheric control of the
669 Madden-Julian Oscillation. *Journal of Climate*, *30*(6), 1909-1922.
670 <https://doi.org/10.1175/Jcli-D-16-0620.1>
- 671 Thompson, D. B., & Roundy, P. E. (2013). The relationship between the Madden-Julian
672 Oscillation and US violent tornado outbreaks in the spring. *Monthly Weather Review*,
673 *141*(6), 2087-2095. <https://doi.org/10.1175/Mwr-D-12-00173.1>
- 674 Tippett, M. K. (2014). Changing volatility of U.S. annual tornado reports. *Geophysical Research*
675 *Letters*, *41*(19), 6956-6961. <https://doi.org/10.1002/2014gl061347>
- 676 Tippett, M. K., Sobel, A. H., & Camargo, S. J. (2012). Association of U.S. tornado occurrence
677 with monthly environmental parameters. *Geophysical Research Letters*, *39*(2).
678 <https://doi.org/10.1029/2011gl050368>
- 679 Tippett, M. K., Sobel, A. H., Camargo, S. J., & Allen, J. T. (2014). An empirical relation
680 between U.S. tornado activity and monthly environmental parameters. *Journal of*
681 *Climate*, *27*(8), 2983-2999. <https://doi.org/10.1175/jcli-d-13-00345.1>
- 682 Tippett, M. K., Allen, J. T., Gensini, V. A., & Brooks, H. E. (2015). Climate and hazardous
683 convective weather. *Current Climate Change Reports*, *1*(2), 60-73.
684 <https://doi.org/10.1007/s40641-015-0006-6>

- 685 Vitart, F. (2017). Madden-Julian Oscillation prediction and teleconnections in the S2S Database.
686 *Quarterly Journal of the Royal Meteorological Society*, 143(706), 2210-2220.
687 <https://doi.org/10.1002/qj.3079>
- 688 Wheeler, M. C., & Hendon, H. H. (2004). An all-season real-time multivariate MJO index:
689 Development of an index for monitoring and prediction, *Monthly Weather Review*,
690 132(8), 1917-1932. [https://doi.org/10.1175/1520-](https://doi.org/10.1175/1520-0493(2004)132<1917:Aarmmi>2.0.Co;2)
691 [0493\(2004\)132<1917:Aarmmi>2.0.Co;2](https://doi.org/10.1175/1520-0493(2004)132<1917:Aarmmi>2.0.Co;2)
- 692 Wilks, D. S. (2006), *Statistical Methods in the Atmospheric Sciences, Int. Geophys. Ser.*, 2nd ed.,
693 vol. 91, U.S.A.: Academic Press.
- 694 Zhang, C. (2013). Madden–Julian Oscillation: Bridging weather and climate. *Bulletin of the*
695 *American Meteorological Society*, 94(12), 1849-1870. [https://doi.org/10.1175/BAMS-D-](https://doi.org/10.1175/BAMS-D-12-00026.1)
696 [12-00026.1](https://doi.org/10.1175/BAMS-D-12-00026.1)



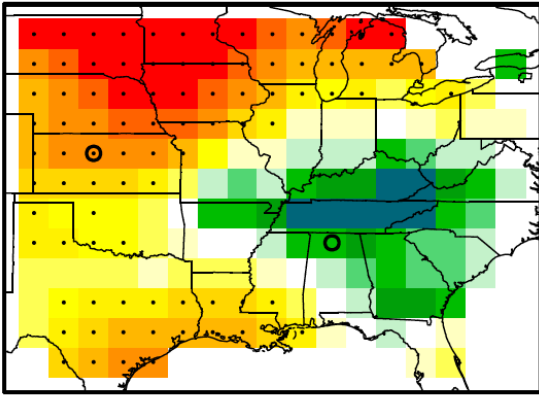
697

698 **Figure 1.** The climatological number of **(a)** tornado events and **(b)** hail events per year are
699 shown, averaged over the years 1979–2015 for each $1.5^\circ \times 1.5^\circ$ grid box. The Plains and the
700 Southeast are delimited by solid white and dashed white lines, centered at $(261^\circ\text{E}, 39^\circ\text{N})$ and
701 $(273^\circ\text{E}, 34.5^\circ\text{N})$, respectively. **(c-d)** Smoothed seasonal cycles of CAPE (red), SRH (blue),
702 CSRH2 (violet), tornado events (solid black), and hail events (dashed black) are shown,
703 computed over the **(c)** Plains and **(d)** Southeast. The season of interest, MAMJ, is shaded in light
704 brown. The seasonal cycle for each variable has been normalized by its respective annual
705 maximum. For the Plains, the annual maxima for CAPE, SRH, CSRH2, tornado events, and hail
706 events are 871 J kg^{-1} , $131 \text{ m}^2 \text{ s}^{-2}$, $1.00 \times 10^7 \text{ m}^6 \text{ s}^{-6}$, $0.710 \text{ events day}^{-1}$, and $3.11 \text{ events day}^{-1}$,
707 respectively; for the Southeast, they are 868 J kg^{-1} , $142 \text{ m}^2 \text{ s}^{-2}$, $4.56 \times 10^6 \text{ m}^6 \text{ s}^{-6}$, $0.413 \text{ events day}^{-1}$,
708 1 , and $1.68 \text{ events day}^{-1}$, respectively.

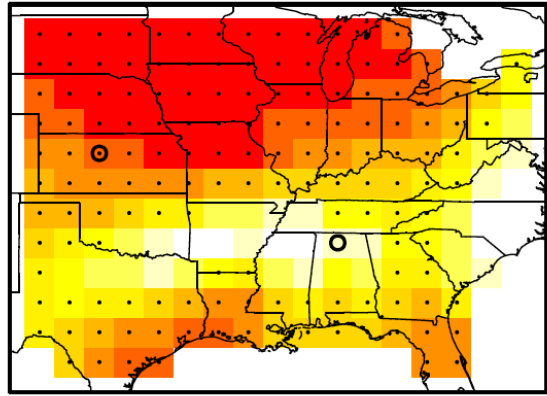


710 **Figure 2.** Weekly composites of anomalous **(a,f)** CAPE, **(b,g)** SRH, **(c,h)** CSRH2, **(d,i)** tornado
711 events, and **(e,j)** hail events for the **(a-e)** Plains and **(f-j)** Southeast are plotted. For example, the
712 maximum in SRH in **(g)** at a lead time of 4 weeks following phase 4 of the MJO represents the
713 weekly averaged value of anomalous SRH for lead times spanning 22–28 days; while the
714 maximum value in tornado events in **(d)** at a lead time of 2 weeks following phase 2 of the MJO
715 represents the weekly summed value of anomalous tornado events for the lead times spanning 8–
716 15 days. Percentages indicate a given anomaly’s deviation from its March-July climatological
717 value. Pattern means are removed before plotting. In Figure S1, we display Figure 2 with its
718 statistical significance plotted and the plotting function’s smoothing turned off.

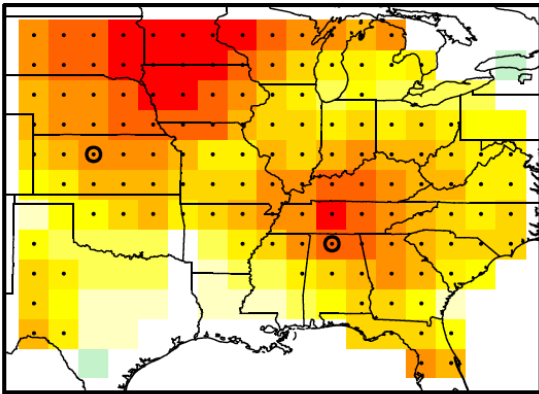
a tornado events versus CAPE



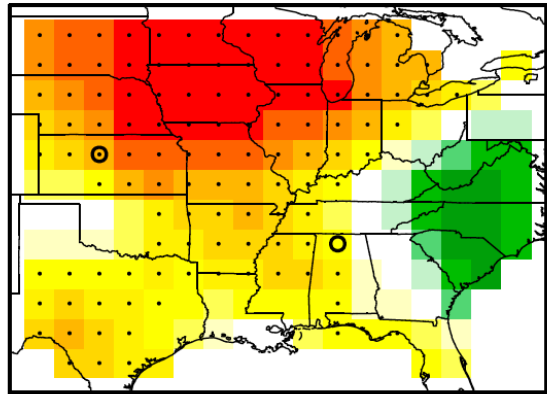
b hail events versus CAPE



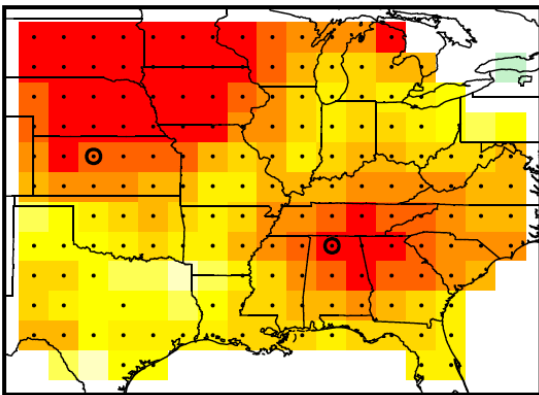
c tornado events versus SRH



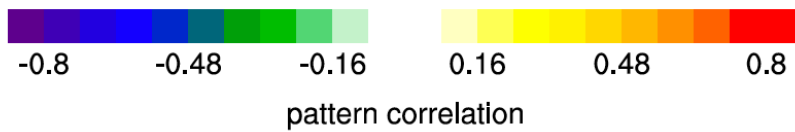
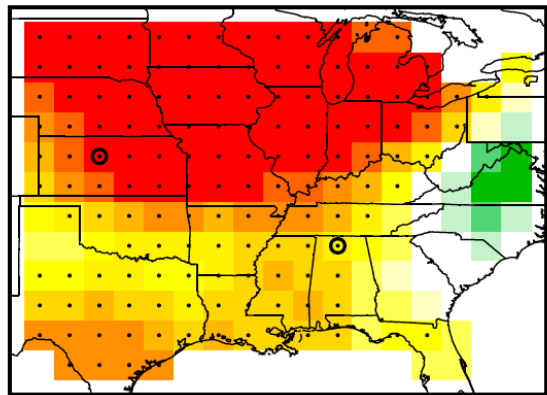
d hail events versus SRH



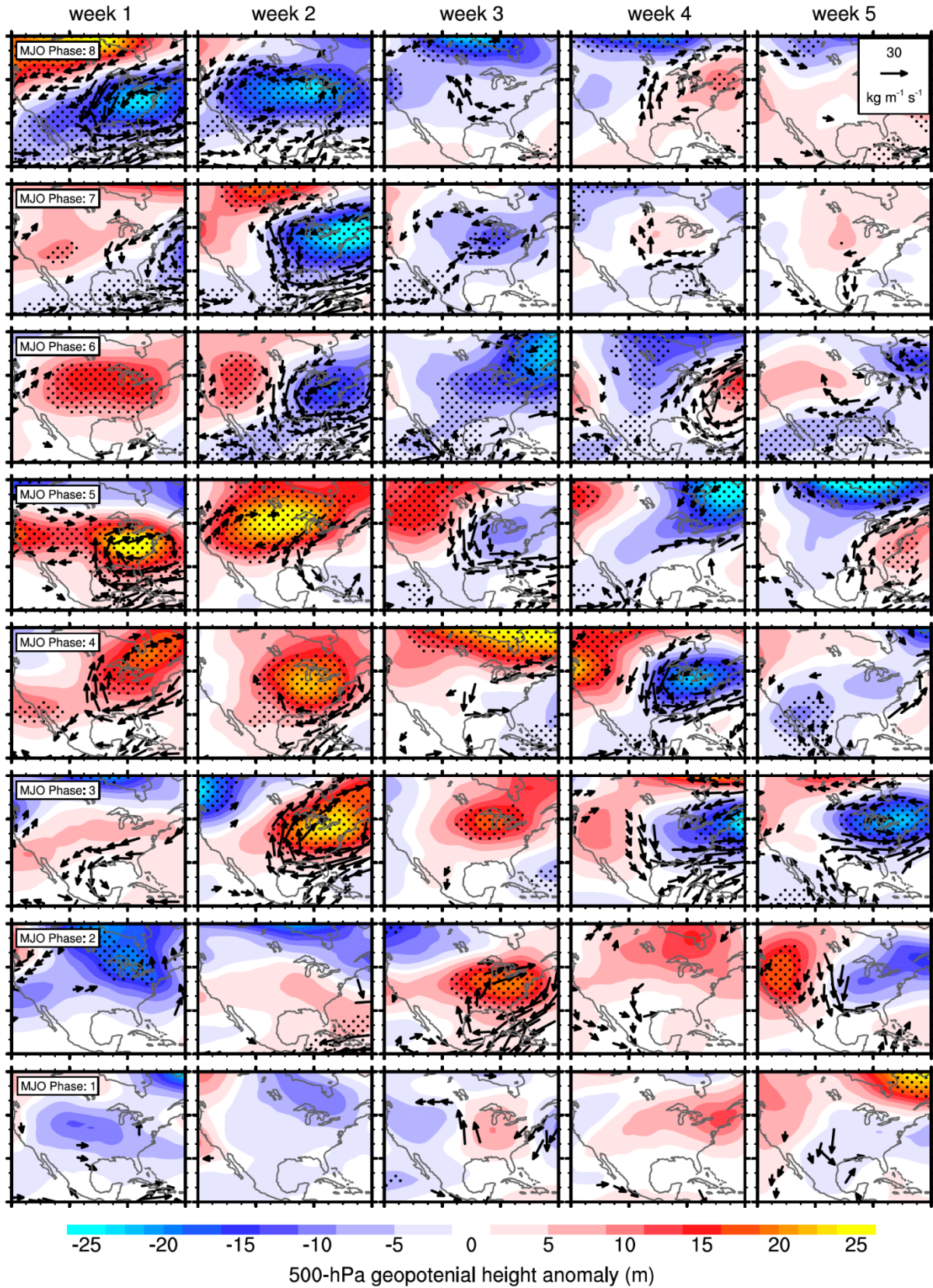
e tornado events versus CSRH2



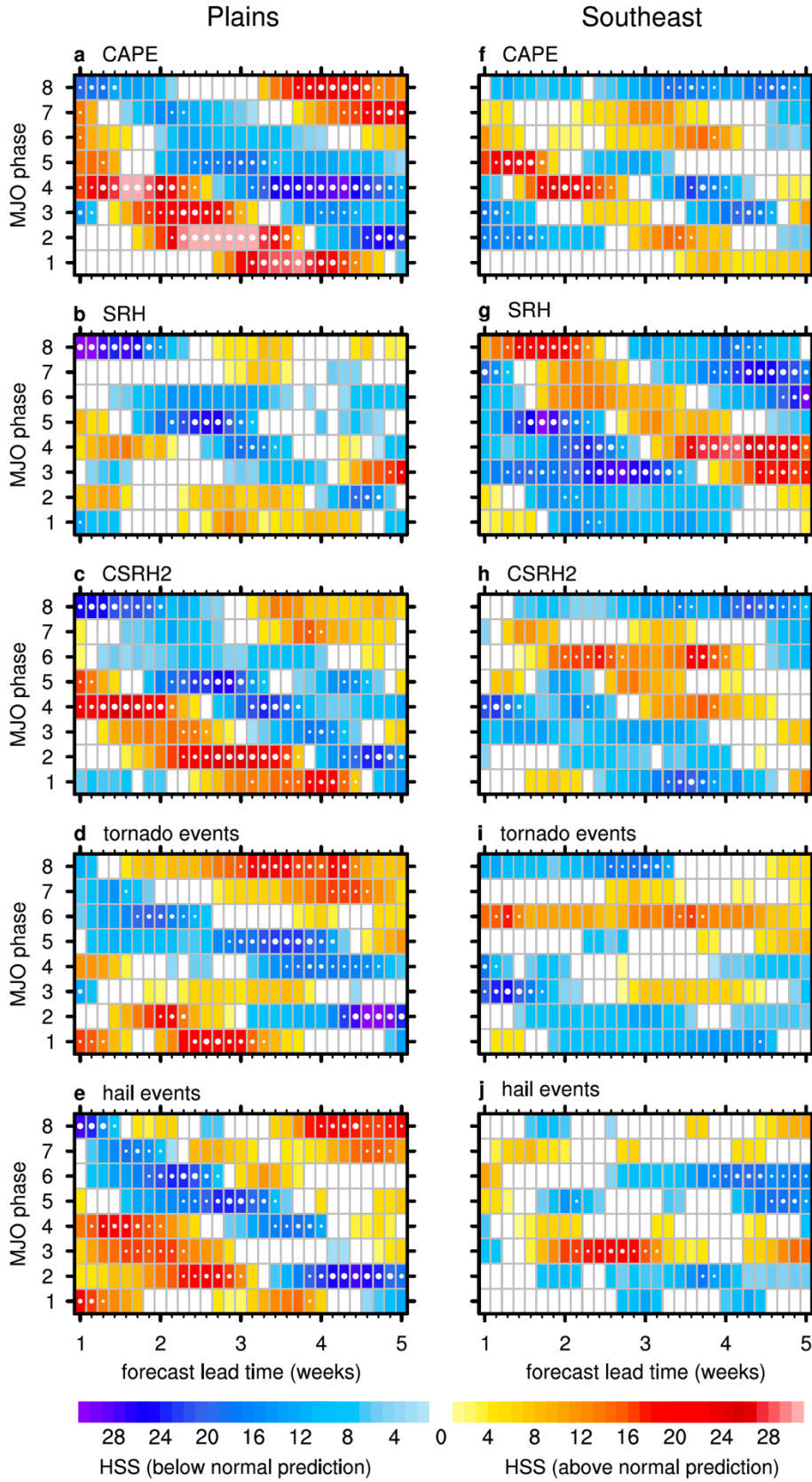
f hail events versus CSRH2



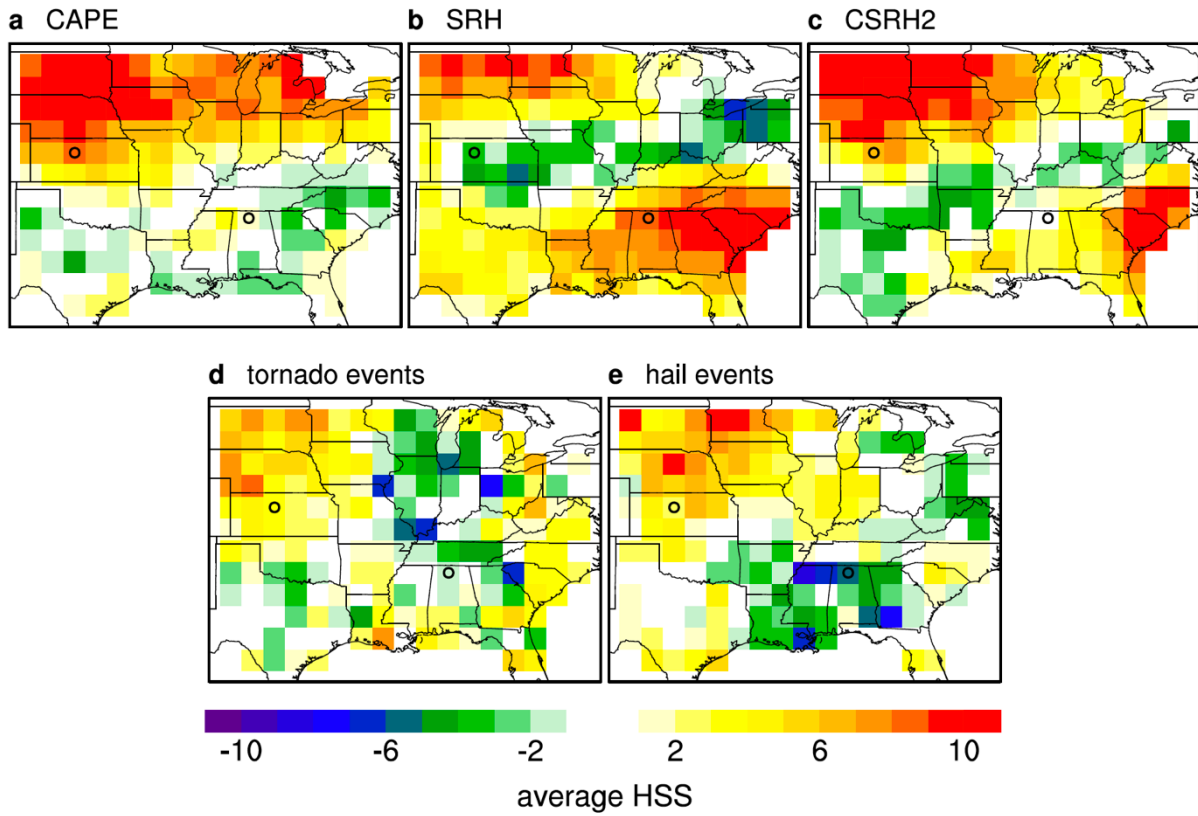
720 **Figure 3.** Centered pattern correlations that are calculated across 8 MJO phases and 31 lead
721 times are shown for (a) tornado events versus CAPE, (c) tornado events versus SRH, (e) tornado
722 events versus CSRH2, (b) hail events versus CAPE, (d) hail events versus SRH, and (f) hail
723 events versus CSRH2. The open black circles highlight the pattern correlations discussed in the
724 text for the Plains and the Southeast, as derived from the composites in Figure 2. The remaining
725 values represent the pattern correlations between the composites that are calculated for each
726 overlapping $7.5^\circ \times 7.5^\circ$ region, centered every 1.5° in longitude from 258.0°E to 282.0°E and
727 every 1.5° in latitude from 28.5°N to 45.0°N . We only display values for regions who central
728 grid box overlap the landmass of the United States. Statistical significance is assessed via a
729 bootstrapping method that accounts for autocorrelation (see Section 2.6). Each black dot
730 indicates that a given pattern correlation exceeds 95% of 1000 randomly generated pattern
731 correlations. The random pattern correlations are generated by producing random composites of
732 tornado and hail events (across MJO phase and lead time space) and then calculating their
733 pattern correlations with the observed composites of CAPE, SRH, and CSRH2.



735 **Figure 4.** Composites of anomalous, weekly averaged 500-hPa heights (m) and vertically
 736 integrated vapor transport (IVT; $\text{kg m}^{-1} \text{s}^{-1}$) are shown. From top to bottom, the rows correspond
 737 to MJO phases 8 through 1, respectively. From left to right, the columns correspond to lead
 738 weeks 1 through 5, respectively. Each panel encompasses a longitudinal range of 235.0°E to
 739 295.0°E and a latitudinal range of 15.0°N to 60.0°N. Black vectors depict anomalous IVT, where
 740
$$IVT = \mathbf{i} \left(\frac{1}{g} \int_{1000 \text{ hPa}}^{300 \text{ hPa}} u q dp \right) + \mathbf{j} \left(\frac{1}{g} \int_{1000 \text{ hPa}}^{300 \text{ hPa}} v q dp \right).$$
 Here, u is zonal wind, v is meridional wind,
 741 q is specific humidity, dp is the difference between reanalysis pressure levels, and g is the
 742 acceleration of gravity; \mathbf{i} and \mathbf{j} represent the unit vectors in the zonal and meridional directions,
 743 respectively. Statistical significance is assessed via a bootstrapping method that accounts for
 744 autocorrelation (see Section 2.6). The method produces a distribution of 1000 random
 745 composites for each component of IVT and 500-hPa heights that vary according to MJO phase
 746 and lead week. Only composited anomalous IVT vectors with magnitudes exceeding $10 \text{ kg m}^{-1} \text{ s}^{-1}$
 747 and having either component statistically significant at the 95% confidence level are plotted.
 748 Stippling denotes where the 500-hPa heights anomalies are significant at the 95% confidence
 749 level. A two-tailed test is employed.



751 **Figure 5.** Heidke skill scores of the empirical prediction model are shown for **(a,f)** CAPE, **(b,g)**
752 SRH, **(c,h)** CSRH2, **(d,i)**, tornado events, and **(e,j)** hail events for the **(a-e)** Plains and **(f-j)**
753 Southeast. Regions shaded in color have positive skill scores; regions shaded in white have
754 negative skill scores. Warm and cool colors indicate predictions of above and below normal
755 activity, respectively. Statistical significance is conveyed by small, medium, and large white dots
756 for predictions that are more skillful than 80%, 90%, and 95%, respectively, of 1000 random
757 forecast samples generated by a bootstrapping technique that accounts for autocorrelation (see
758 Section 2.6).



759

760 **Figure 6.** Heidke skill scores that are averaged across 8 MJO phases and 29 lead times for the
761 empirical prediction of **(a)** CAPE, **(b)** SRH, **(c)** CSRH2, **(d)** tornado events, and **(e)** hail events
762 are shown. The open black circles represent the average skill scores for the Plains and the
763 Southeast, as derived from Figure 5. The remaining values represent the averages for each
764 overlapping $7.5^\circ \times 7.5^\circ$ region, centered every 1.5° in longitude from 258.0°E to 282.0°E and
765 every 1.5° in latitude from 28.5°N to 45.0°N . We only display values for regions who central
766 grid box overlap the landmass of the United States. Before being averaged, the individual skill
767 scores are weighted by the sample size of its corresponding MJO phase (see Table S1).